
Article:
Perejon, A., Gil-Gonzalez, E., Sanchez-Gimenez, P. et al. (2 more authors) (2018) Electrical properties of bismuth ferrites:Bi2Fe4O9 and Bi25FeO39. Journal of the European Ceramic Society. ISSN 0955-2219

https://doi.org/10.1016/j.jeurceramsoc.2018.09.008

Electrical properties of bismuth ferrites: $Bi_2Fe_4O_9$ and $Bi_{25}FeO_{39}$

Antonio Perejón[a,b,*], Eva Gil-González[a], Pedro E. Sánchez-Jiménez[a], Anthony R. West[c], Luis A. Pérez-Maqueda[a,*]

[a] Instituto de Ciencia de Materiales de Sevilla (C.S.I.C.-Universidad de Sevilla). C. Américo Vespucio 49, Sevilla 41092. Spain

[b] Departamento de Química Inorgánica, Facultad de Química, Universidad de Sevilla, Sevilla 41071, Spain

[c] Department of Materials Science and Engineering, University of Sheffield, Sheffield, S1 3JD, UK.

Abstract

$Bi_2Fe_4O_9$ was prepared by solid-state reaction and the electrical properties measured by impedance spectroscopy. After annealing in O_2 at 900 ºC, $Bi_2Fe_4O_9$ is an electronically-homogeneous insulator. Its high frequency permittivity is constant over the temperature range 300-400 ºC and shows no evidence of incipient ferroelectricity at lower temperatures. On annealing in N_2 at 900 ºC, the sample gradually decomposes.

$Bi_{25}FeO_{39}$ was prepared by both solid-state reaction and mechanosynthesis. It showed a modest amount of mixed conduction of both oxide ions and holes. Impedance analysis showed a complex response that best fitted an equivalent circuit consisting of a parallel combination of long-range conduction and short range dielectric relaxation elements.

The electrical conductivity of both $Bi_2Fe_4O_9$ and $Bi_{25}FeO_{39}$ is less than that of $BiFeO_3$ prepared by solid-state reaction, which indicates that any leakage conductivity of $BiFeO_3$ is not due to the possible presence of small amounts of these secondary phases.

Keywords: $Bi_2Fe_4O_9$; mullite; $Bi_{25}FeO_{39}$; sillenite; $BiFeO_3$

**Corresponding authors:*

antonio.perejon@icmse.csic.es

maqueda@cica.es

1. Introduction

There is much interest in $BiFeO_3$ for its multiferroic properties [1-8]. However, applications so far have been limited because most samples prepared by solid-state reaction show significant levels of electronic conductivity [8-11]. Controversy remains concerning both the magnitude and mechanism of its conductivity. Some authors attribute the electronic conductivity to a mixed valence state of Fe associated perhaps with oxygen deficiency [9-13]; others attribute it to the presence of secondary phases $Bi_{25}FeO_{39}$ and/or $Bi_2Fe_4O_9$ [14-15]. Synthesis of phase-pure $BiFeO_3$ by solid state reaction of oxide mixtures is notoriously difficult and secondary phases are difficult to eliminate [16-17]. By contrast, $BiFeO_3$ prepared by mechanosynthesis is phase-pure, insulating and exhibits all the expected characteristic multi-ferroic properties [18-20].

$Bi_{25}FeO_{39}$ has a cubic structure, space group I23, characteristic of sillenites [21]. On heating, it is reported to decompose at 777 ºC [22]. Some authors claim that its chemical formula is, instead, $Bi_{25}FeO_{40}$ but there is no reported clear evidence for the partial stabilization of Bi^{5+} implied by this formula [23-25]. $Bi_{25}FeO_{39}$ shows photocatalytic activity under ultraviolet and visible light irradiation [26-27] and photochromic properties have been reported in single crystals [28]. The magnetic properties of $Bi_{25}FeO_{39}$ are unclear. Some authors showed paramagnetic behavior between 5 K and 950 K [24, 29], while others suggested either ferri- or ferro-magnetic behavior [22, 30]. To the best of our knowledge, the electrical properties of $Bi_{25}FeO_{39}$ have not yet been studied.

$Bi_2Fe_4O_9$ is orthorhombic, space group Pbam, with a mullite structure [31]. It is antiferromagnetic with a Néel temperature of 264 K [32-33]. It is also claimed to be multiferroic [32-37]: antiferromagnetic order stems from partially-filled d-orbitals of Fe [38] and the stereochemically-active electron lone pair on Bi could perhaps favour a ferroelectric distortion in its crystal structure. However, the evidence for ferroelectricity is not strong. Hysteresis data have been reported [32, 34, 39] in which the polarization-electric field curves tend to give oval rather than ferroic-shaped hysteresis loops and in one report [39], it was stated that the P-E curves were 'characteristic of very poor ferroelectric materials'. $Bi_2Fe_4O_9$ presents catalytic activity under visible light irradiation [40-41], with a band gap of about 1.53 eV [42].

One objective of the present work was to measure the electrical properties of phase-pure samples of $Bi_2Fe_4O_9$ and $Bi_{25}FeO_{39}$ and determine whether, as secondary phases, they could perhaps contribute to the electrical properties of semiconducting $BiFeO_3$. It was also of interest to measure their electrical properties to test for possible oxide ion conduction and dielectric relaxation effects in $Bi_2Fe_4O_9$, and to measure the permittivity of $Bi_{25}FeO_{39}$ since some other sillenites have been reported to show relaxor behaviour.

2. Materials and Methods

Both compositions were prepared from commercial Bi_2O_3 (Sigma-Aldrich 223891-500G, 99.9% purity) and Fe_2O_3 (Sigma-Aldrich 310050-500G, ≥99% purity), which were used as-received. $Bi_{25}FeO_{39}$ was prepared by both solid-state reaction and direct mechano-synthesis. For the latter, samples were milled under 7 bar of O_2 pressure in a Pulverisette 7 planetary mill (Fritsch, Idar-Oberstein, Germany), which had been modified to operate under different atmospheres at high pressures. Hardened steel jars (80 cm^3 volume) and balls (9 balls, 15 mm diameter) were used. The powder-to-ball mass ratio was set at 1:20 and the spinning rate of the supporting disc and the superimposed rotation of the jars in the opposite direction was set at 700 rpm. The milling time was 15 h. Cold-pressed pellets were prepared using a uniaxial press and sintered in air at 750 ºC for 0.5 h.

$Bi_{25}FeO_{39}$ and also $Bi_2Fe_4O_9$ were prepared by conventional solid-state reaction from oxide raw materials which were mixed in an agate mortar. Pellets were cold-pressed and reaction-sintered at 900 ºC for 10 h (for $Bi_2Fe_4O_9$) and at 750 ºC for 30 min (for $Bi_{25}FeO_{39}$) in air in alumina crucibles. Subsequent impedance measurements on $Bi_2Fe_4O_9$ indicated the possibility of partial reduction of samples heated in air and therefore, a series of samples was also prepared which were given a final heating in either O_2 or N_2 at 900 ºC for different times prior to impedance measurements.

XRD patterns were collected on powdered samples of either reacted powders or crushed, sintered pellets using a Panalytical X'Pert Pro diffractometer working at 45 kV and 40 mA, CuKα radiation and equipped with an X'Celerator detector. Rietveld refinements were carried out with FullProf software. The background was refined using a sixth order polynomial function, and a pseudo-Voigt profile function with axial divergence asymmetry to refine peak shapes. Peak shapes, lattice parameters and scale factor were refined simultaneously. Atomic positions and isotropic temperature factors were subsequently included in the refinement. The microstructure of pelleted samples was analyzed by scanning electron microscopy (SEM) using a Hitachi S-4800 microscope. Cross-sections of the pellets were thermally etched for 30 min at 90% of the corresponding sintering temperature to reveal the grain boundaries. For electrical property measurements, reacted powders were pressed into disks ~6 mm diameter by uniaxial pressing at 0.93 GPa and sintered. The density of the pellets was measured by the Archimedes' method, using distilled water at room temperature as the immersion liquid. Electrodes were fabricated from sputtered gold using a Cressintong Sputter 108auto. Electroded samples were connected to the platinum wires of a conductivity jig, which was placed into a horizontal tube furnace. The atmosphere inside the jig could be varied between oxygen, air and nitrogen. The electrical properties of samples were characterized by impedance spectroscopy, taking into account the blank capacitance of the conductivity jig and the overall pellet geometry. The impedance

measurements were taken using a Newtons4th Ltd impedance analyser (Loughborough, UK) over the frequency range 1 Hz to 1 MHz, with an *ac* measuring voltage of 0.1 V. A *dc* bias of 50 V cm^{-1} was applied during some measurements.

3. Results and Discussion

3.1. $Bi_2Fe_4O_9$

$Bi_2Fe_4O_9$, with a mullite structure, was prepared phase-pure by solid state reaction. XRD data of a crushed pellet are shown in Fig. S1; the data were analyzed by Rietveld refinement with final parameters shown in Table S1, which also confirmed the absence of any secondary phases. For the Rietveld refinement, input crystallographic data were obtained from the literature [43]; the refined coordinates, Table S1 were essentially the same as reported and confirm the mullite structure of $Bi_2Fe_4O_9$. A SEM micrograph is shown in Fig. 1. Grain size was 0.1-0.5 μm. The pellet density was determined by the Archimedes' method to be 95%.

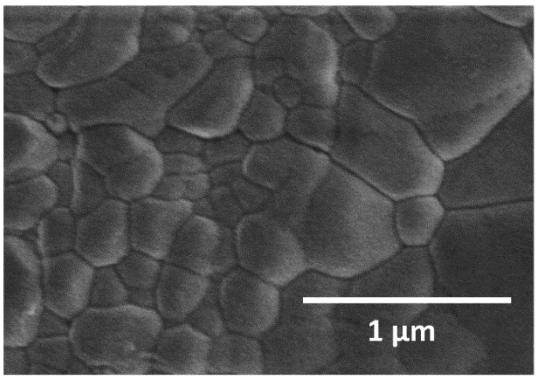

Fig. 1. SEM micrograph of the cross-section of a pellet of $Bi_2Fe_4O_9$ reaction-sintered at 900 ºC for 10 h in air.

Impedance data for samples annealed in air, O_2 and N_2 (referred to here as the air, O_2 and N_2 samples) at 900 ºC were measured in air, apart from the samples heated in N_2, which were measured in N_2. Impedance measurements were made over the temperature range room temperature to 400 ºC. A selection of results is shown in Figs. 2(O_2), 3(air) and 4(N_2).

The impedance complex plane plots (a) show a single arc for all three samples but replotting the same data as combined Z''/M'' spectroscopic plots (b) shows the appearance of an additional high frequency effect, especially for the N_2 sample, in the M" plots. The Z''/M'' plots show a single peak with almost coincident frequency for O_2 and air samples, Figs. 2,3(b) which indicates

that the samples were electrically homogeneous. The small offset in peak positions is attributed to the non-ideality of the impedance data which requires inclusion of a constant phase element, CPE for accurate circuit fitting, discussed later. The N_2 sample, Fig. 4(b) however, shows non-overlapping Z''/M'' peaks and a turn-up in M'' at high frequencies which, taken together, indicate that the N_2 sample was no longer homogeneous.

The single peak in the M'' plot of the O_2 sample, Fig. 2(b) corresponds to the component with the smallest capacitance which therefore, represents the sample bulk. The overlapping Z'' peak and the corresponding arc in the impedance complex plane plot, (a), also represent the bulk resistance. Impedance data for the O_2 sample fitted accurately the equivalent circuit shown in Fig. 5(a), inset; fits to C', Z'' vs Z', Y' and M'' / Z'' are given in (a-d), fitting residuals in (e) and summarized fit parameters for five temperatures in Table 1. An Arrhenius plot of the bulk conductivity, R_1^{-1}, Fig. 5(f) is linear with activation energy 1.19(1) eV. Stoichiometric $Bi_2Fe_4O_9$ is therefore a modest electronic conductor with a conductivity of eg. 2.77×10^{-7} Scm^{-1} at 350 ºC. There was no evidence from the low frequency capacitance data, Fig. 5(a) for any ionic conduction: if oxide ion conduction were present, this should give rise to high sample-electrode capacitances in the range 1-10 μF, whereas experimental C' data did not exceed 3-100 pF, Figs. 2-5.

C' data, Fig. 2(c), show a high frequency plateau with a value in the range 1.25-1.29 $pFcm^{-1}$. This corresponds to the limiting high frequency permittivity of the sample, ε'_∞ (calculated using the equation $\varepsilon_\infty' = C_\infty/e_0$ where $e_0 = 8.854 \times 10^{-14}$ Fcm^{-1}) with a typical value of 14.1; values of ε'_∞ as a function of temperature are summarized in Table 1: C_∞ is represented by the element C_1 in Fig 5(a), inset. The values of ε'_∞ are independent of temperature over the range 300-400 ºC, Table 1, and show no evidence for a decrease with increasing temperature which could be interpreted as Curie-Weiss behavior, indicative of a phase transition to a ferroelectric structure at some lower temperature. We therefore find no evidence for possible multi-ferroic behavior at lower temperatures of $Bi_2Fe_4O_9$.

The C' data at frequencies below the C_∞ plateau, Fig. 2(c), show a small linear increase which indicates a departure from the frequency-independent behaviour expected for an ideal parallel RC element. This was modelled by inclusion of the constant phase element, CPE_1 in the circuit element that represents the bulk impedance of the sample. Similarly, the high frequency dispersion in Y' data, Fig.5(c) are modelled by CPE_1.

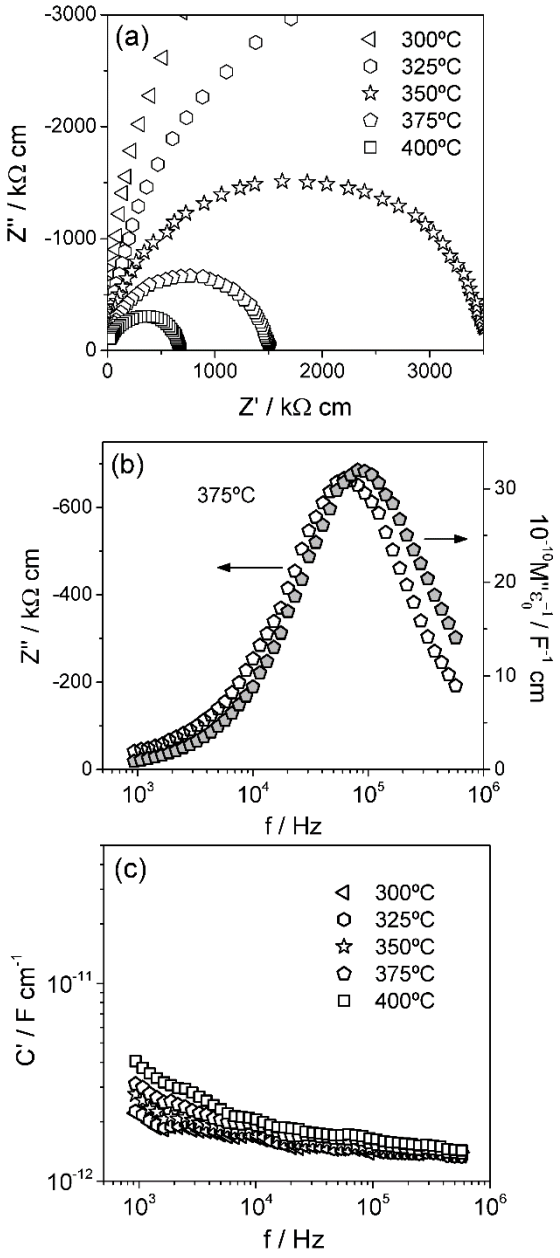

Fig. 2. Impedance data over the temperature range 300-400ºC for $Bi_2Fe_4O_9$ annealed in O_2. (a) Impedance complex plane plots, (b) Z"/M" spectroscopic plots at 375 ºC, (c) C' spectroscopic plots.

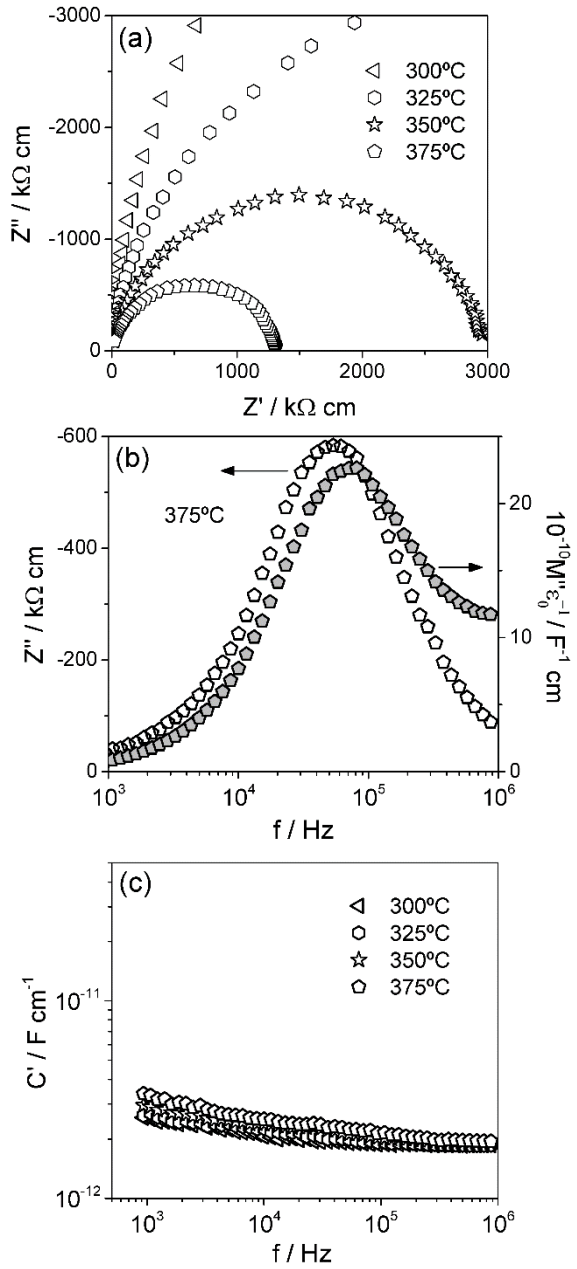

Fig. 3. Impedance data over the temperature range 300-375ºC for $Bi_2Fe_4O_9$ reaction-sintered at 900 ºC for 10 h in air. (a) Impedance complex plane plots, (b) Z"/M" spectroscopic plots at 375 ºC, (c) C' spectroscopic plots.

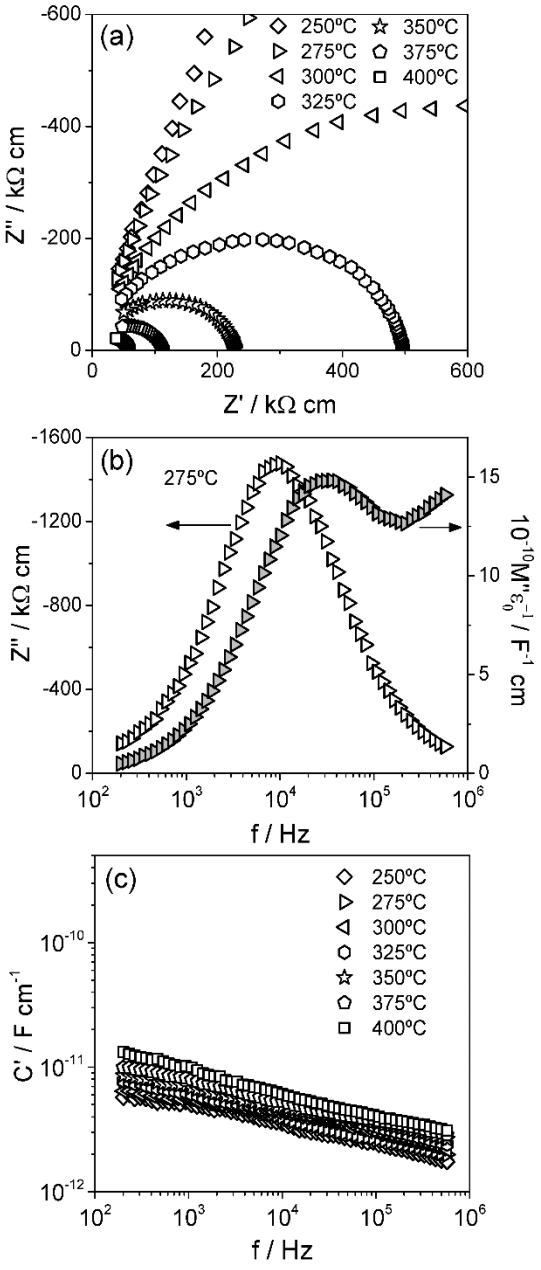

Fig. 4. Impedance data over the temperature range 250-400ºC for $Bi_2Fe_4O_9$ annealed in N_2 for 1 h. (a) Impedance complex plane plots, (b) Z"/M" spectroscopic plots at 275 ºC, (c) C' spectroscopic plots.

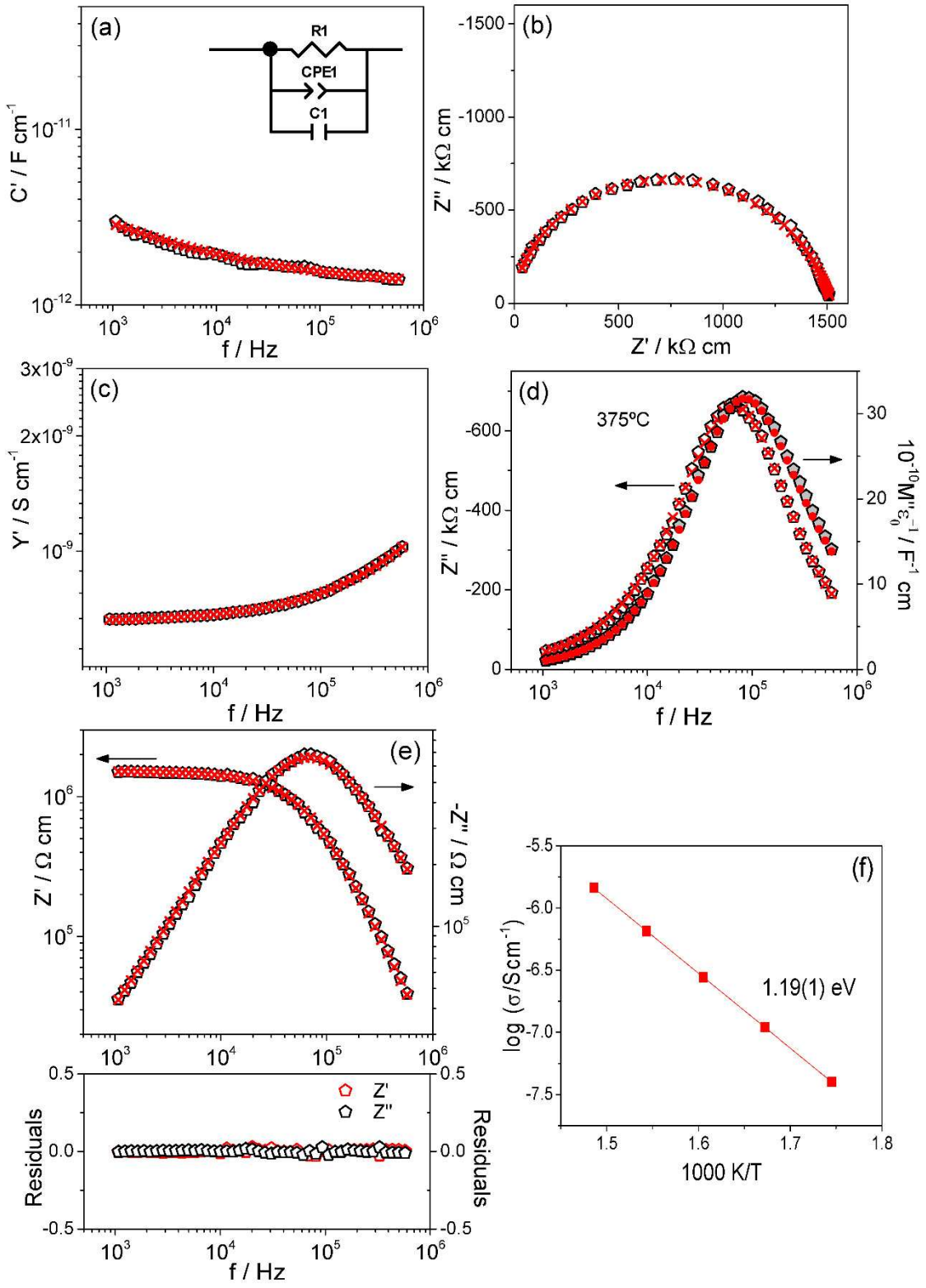

Fig. 5. Fitted and experimental impedance data measured at 375 ºC for $Bi_2Fe_4O_9$ annealed in O_2. (a) C' spectroscopic plot, (b) impedance complex plane plot, (c) Y' spectroscopic plot, (d) Z"/M" spectroscopic plots, (e) Z'/Z" spectroscopic plots and residuals, (f) Arrhenius plot for R_1.

Table 1. Fitted parameters for the equivalent circuit shown in Fig. 5(a), inset, used to simulate the impedance data for $Bi_2Fe_4O_9$ reaction-sintered at 900 ºC for 10 h in air.

T (ºC)	**300**	**325**	**350**	**375**	**400**
R_1 (kΩcm)	2.50(5)x10^4	9.08(5)x10^3	3.61(1)x10^3	1.53(1)x10^3	686(1)
A_1 (pScm^{-1}rad^{-n})	24(9)	30.8(9)	40(1)	52(2)	60(2)
n_1	0.63(3)	0.63 (fixed)	0.63 (fixed)	0.63 (fixed)	0.63 (fixed)
C_1 (pFcm^{-1})	1.29(3)	1.25(1)	1.25(1)	1.25(1)	1.27(1)
ε'_∞	14.6(3)	14.2(1)	14.1(1)	14.1(1)	14.3(1)

Figure S2 shows the dependence of the impedance response of $Bi_2Fe_4O_9$ on either (a) atmosphere (N_2, air and O_2 after equilibrating the system for 45 min) surrounding the O_2 sample or (b) an applied *dc* bias. The conductivity is essentially independent of both pO_2 and applied *dc* bias, which indicates that the modest level of electronic conductivity of the sample is intrinsic.

Impedance data for the air and, especially N_2, samples, however, showed evidence for electrical inhomogeneity that may be associated with a small amount of oxygen loss. The M'' spectra show the onset of a peak(s) at higher frequency, Fig. 4(b), which is of low relative resistance since it does not appear in the corresponding Z'' spectra. This may be attributed to oxygen loss according to:

$$O^{2-} = 1/2O_2 + 2e^-$$

and the creation of extrinsic, n-type semi-conduction. After annealing in O_2, the changes that were caused by heating for 5 h in N_2 were reversible and the high frequency M'' anomalies disappeared. After longer times at 900 ºC in N_2, however, the effects may be irreversible since XRD of pellet surfaces showed the appearance of a small amount of Fe_2O_3, which increased with annealing time in N_2, Fig. S3. It appears therefore, that $Bi_2Fe_4O_9$ is stable at 900 ºC only in the presence of an oxidizing atmosphere.

The impedance data for the N_2 sample, Fig. 4, show a distorted arc, especially for long annealing times, from which the total resistances were extracted and are shown, together with data for the O_2 sample, in Fig. 6 as conductivity Arrhenius plots. With increased annealing time in N_2, the overall conductivity increased; it is not clear whether this was due to the presence of conducting Fe oxides, to oxygen loss from $Bi_2Fe_4O_9$ or to a combination of both effects. It is also not clear whether decomposition of Bi_2FeO_9 in atmospheres of lower pO_2 at 900 ºC was due to loss of Bi_2O_3 by evaporation from the sample, although if this were the case, it should presumably be independent of pO_2. Alternatively, the sample may start to lose oxygen in low pO_2 which then catalyzed the loss of Bi.

The M" plots for the air and N_2 samples showed the onset of a second, high frequency peak, Fig. 3,4(b). Although only limited data on this element are available, it was possible to estimate its resistance, labelled R_{hf} and temperature-dependence. The Arrhenius plot for the air sample, Fig. S4, shows linear data for R_1 with activation energy 1.12 eV, but a small and almost temperature-independent resistance for R_{hf}. We tentatively attribute R_{hf} to a thin layer of iron oxide, probably at grain surfaces, which acts as a low resistance series pathway between the more resistive, fully oxidised $Bi_2Fe_4O_9$ grains. However, the amount of iron oxide formed was too small to detect by XRD: Rietveld refinement of the air sample, Table S1, showed 100 wt % of the $Bi_2Fe_4O_9$ main phase. We have not study any further the decomposition of $Bi_2Fe_4O_9$.

We are aware of only one other paper that reports impedance measurements of $Bi_2Fe_4O_9$ [42]. Samples were sintered at 950 °C, probably in air and show various characteristics of the air and N_2 samples measured here. Specifically, M" plots showed a high frequency tail similar to that in Fig 3(b) and an Arrhenius plot with similar activation energy to the N_2 samples shown in Fig. 6. However, the conductivities reported in [42] were attributed to the presence of oxygen vacancies for which we find no evidence from the C' data, Figs. 3,4(c).

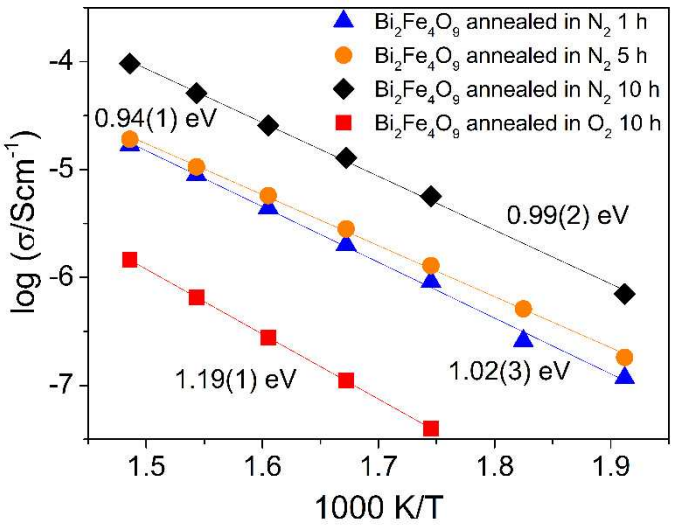

Fig. 6. Arrhenius plots for $Bi_2Fe_4O_9$ annealed in O_2 and in N_2 for 1 h, 5 h and 10 h.

In summary, we interpret the impedance data to indicate that conduction in oxygen-stoichiometric $Bi_2Fe_4O_9$ is electronic with no evidence of any ionic conductivity; the sample-electrode contact with Au electrodes has a negligible resistance in comparison with the high sample resistance. The high frequency bulk permittivity has a value of 14.1 typical of dielectric materials, with no evidence of incipient ferroelectricity. $Bi_2Fe_4O_9$ is stable in O_2 at 900 °C but gradually decomposes in atmospheres of lower pO_2 as shown by an increase in overall conductivity, the appearance of a high frequency conducting element with zero activation energy and the gradual appearance of Fe_2O_3 in XRD data.

3.2. $Bi_{25}FeO_{39}$

Phase-pure samples of $Bi_{25}FeO_{39}$ with the sillenite structure were prepared by both mechanosynthesis and solid state reaction. Powder XRD data, Fig. S5 and Table S1 show the single phase nature of the products. The structure was refined using literature data as starting model and again, the refined coordinates were in good agreement with the literature [44]. Cold-pressed pellets of $Bi_{25}FeO_{39}$ were sintered at 750 ºC; SEM data showing a grain size of 0.1-0.5 μm are presented in Fig. 7; the density was estimated to be 94%.

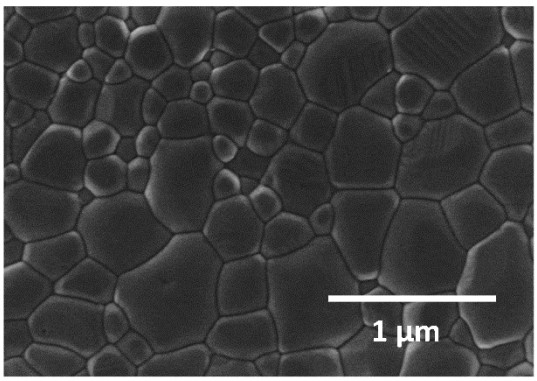

Fig. 7. SEM micrograph of the cross-section of a pellet of $Bi_{25}FeO_{39}$ prepared by mechanosynthesis and sintered at 750 ºC.

Impedance data over the temperature range room temperature-300 ºC are shown in Fig. 8. Similar results were obtained for both sets of samples. The impedance complex plane plot shows, at 200 ºC (a), two poorly-resolved arcs. At temperatures above 250 ºC, a small low frequency tail is observed increasingly and the two arcs merge to give a single asymmetric, distorted arc. Merging of the two arcs is also indicated by the capacitance C' data (b), in which two capacitance plateaux appear at intermediate and high frequencies in the temperature range 200-300 ºC. The high frequency C' plateau is frequency-independent and is clearly seen at the lowest temperatures, with a value of ~4 pF, whereas the intermediate frequency C' plateau is both frequency- and temperature-dependent, with values of ~16 pF and 1 kHz at 200 ºC and ~11 pF and 5 kHz at 250 ºC. The increasing similarity of the two capacitance values with increasing temperature indicates an increasing similarity in the time constants, given by the RC product, of the components responsible for the two plateaux and the arcs seen in the impedance complex plane plots, (a). As the time constant values become more similar, the impedance arcs overlap increasingly because the frequencies at their maxima, ω_{max} given by $\omega_{max}RC=1$ become more similar.

The high frequency C' plateau corresponds to the high frequency component of the distorted arc observed in the impedance complex plane plot (a) and represents the bulk response of the sample. The intermediate frequency C' plateau (b) corresponds to the low frequency component of the distorted arc seen in (a); the possible origin of this capacitance is discussed later. A large increase in capacitance is seen at 250-300 ºC at lower frequencies (b), associated with the tail observed in

the impedance complex plane plots (a). This increase in capacitance at low frequencies reaches values in the μF range and is an indicator of possible ionic conduction.

Figure S6 shows the impedance data at high temperatures (325-400 ºC) for $Bi_{25}FeO_{39}$. The complex plane plots (a) show the main distorted semicircular arc and a small low frequency arc; Z''/M'' spectroscopic plots (b) show single overlapping peaks attributed to the sample bulk response and relaxation, followed by a broad low frequency Z" peak corresponding to the low frequency response of the sample. Capacitance, C' data (c) show two frequency dispersions, above and below 10^3 Hz, leading to the bulk capacitance plateau at higher frequency and to an electrode contact capacitance at lower frequencies.

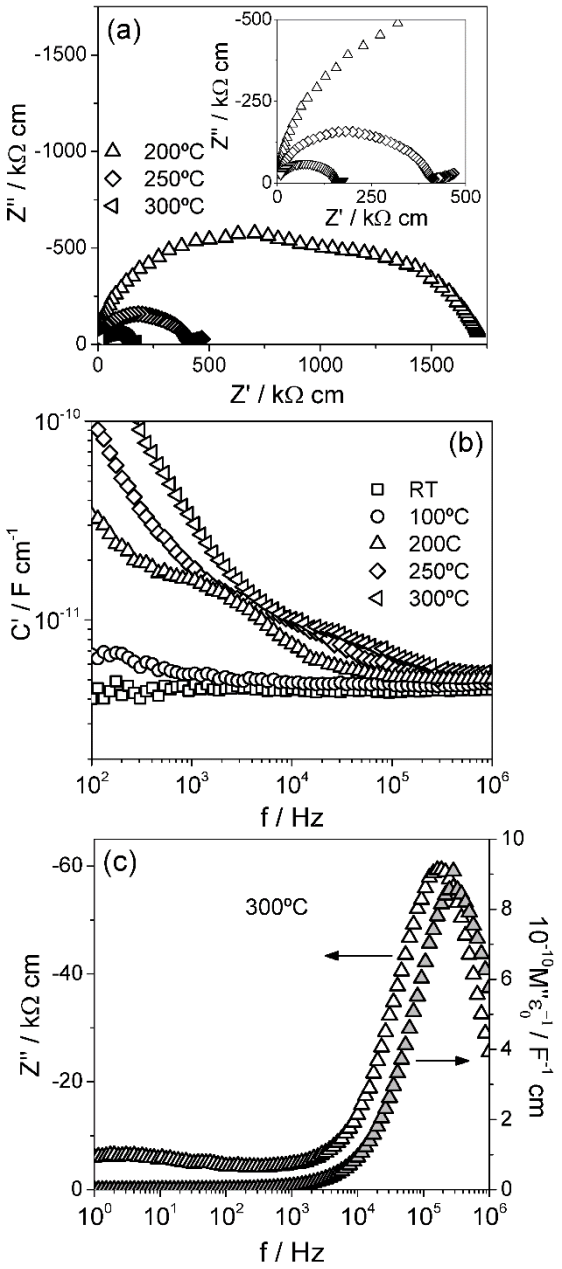

Fig. 8. Impedance data over the temperature range 200-300ºC for $Bi_{25}FeO_{39}$ prepared by mechanosynthesis and sintered at 750ºC. (a) Impedance complex plane plots, (b) C' spectroscopic plots, (c) Z"/M" spectroscopic plots at 300 ºC.

The dependence of the impedance response on atmosphere (N_2, air and O_2) and *dc* bias is shown at 375 ºC in Fig. S7. Both arcs decrease reversibly in size as pO_2 increased (a), which suggests that the electronic component of the overall conduction is p-type. A similar behavior is observed on application of a *dc* bias, since both arcs also decrease in size reversibly (b). It is therefore concluded that $Bi_{25}FeO_{39}$ is both an oxide ion conductor, from the magnitude of the C' values achieved at low frequencies, and a *p*-type semiconductor from the atmosphere- and bias-dependence of the conductivity [45].

The origin of the p-type component of the conductivity is not known. It could be due to a small amount of Fe^{4+} ions in the presence of primarily Fe^{3+} ions in the sillenite structure. Alternatively, it could represent holes trapped on underbonded oxygen as O^- ions [45] or a small amount of Bi^{5+} in the presence of predominantly Bi^{3+}. Since there is a significant activation energy for conduction, the holes must be localized on a specific atomic species rather than delocalized in a conduction band.

In order to analyze further the impedance results for $Bi_{25}FeO_{39}$, it was essential to find the most appropriate equivalent circuit to represent the impedance response. In particular, it was necessary to understand the origin of the intermediate frequency capacitance plateau seen in (b) leading to the distorted impedance arc seen in (a). It seemed unlikely that the intermediate frequency C' plateau could correspond to a grain boundary impedance in series with the bulk impedance since its value was only 3-4 times greater than that of the bulk capacitance. If it did represent a grain boundary effect then the grain boundary would constitute a large volume fraction of the entire sample, which is unlikely. This conclusion is based on the assumption that (i) bulk and grain boundaries have similar permittivities and (ii) the capacitance value is inversely proportional to the thickness of the region responsible.

From the low values of the intermediate frequency plateau, it seemed more likely that a parallel circuit was appropriate consisting of a combination of two components that represented long range conduction and dielectric relaxation, Fig. 9 inset. This circuit has been shown recently to model accurately the impedance data of yttria-stabilised zirconia, YSZ, which also showed an intermediate frequency capacitance plateau whose magnitude was too small to attribute to a series-related impedance [46]. A good fit to this circuit was obtained as shown for one data set in Fig. 9; fit parameters are summarized in Table 2 for fits over the temperature range 200-400 ºC.

The circuit shown in (a) requires explanation and justification. The left part represents the sample bulk and is a combination of two features. The elements R_1, C_1 and CPE_1 represent long range conduction. The same element combination is used in Fig 5(a) and is widely used to represent bulk conduction in materials, although some authors prefer to use a simplified circuit that does not contain C_1. The elements R_2 and C_2 represent a dielectric process, such as dipole reorientation, which does not contribute to long range conduction due to the presence of the blocking

capacitance, C_2. In the case of YSZ, the dipoles were attributed to association of oppositely-charged $Y_{Zr}^{'}$ dopants and oxygen vacancies, $V_o^{\cdot\cdot}$.

The right part of the circuit (a) represents the sample-electrode contact. If the sample were exclusively an oxide ion conductor, component R_3 would give the limiting, low frequency conduction through the sample-electrode arrangement, such as would be obtained by *dc* measurements, in parallel with CPE_3 representing a parallel combination of a charge transfer resistance and a blocking capacitance associated with an oxygen-based redox reaction. Alternatively, R_3 may represent an electronic short circuit at the sample-electrode interface, associated with the electronic component of the overall conduction through the sample.

Using the fitted parameter values given in Table 2, Arrhenius conductivity plots for R_1, R_2 and R_3 are shown in Fig 9(f). R_1 represents the overall resistance to long range conduction through the ceramic and consists of a combination of ionic and electronic conduction processes. We have not made transport number measurements to separate the ionic and electronic conductivities but note that the activation energy for R_1, 0.52(2) eV, is significantly less than that ~ 1 eV, of typical good oxide ion conductors such as YSZ. This may be because conduction in $Bi_{25}FeO_{39}$ is primarily electronic or because co-operative interactions between the mobile ionic and electronic species act to reduce the overall activation energy.

The R_2-C_2 combination, Fig. 9(a), represents a dielectric relaxation process in which R_2 is confined to local charge displacements. There are several possible origins of this effect. It could represent reorientation of trapped ionic dipoles, such as have been proposed in YSZ [46]. It may also represent reorientation of trapped electronic dipoles whose nature is unknown. A third possibility is that $Bi_{25}FeO_{39}$ has, at these measurement temperatures, a residual fluctuating domain structure associated with either incipient ferroelectric or relaxor behavior at lower temperatures. R_2 would therefore represent the resistance to domain reorientation. This possibility is supported by the values of C_2, Table 2, which decrease with increasing temperature, as occurs with ferroelectric materials in the Curie-Weiss region above their Curie temperature.

We note that a similar effect has been seen in the stoichiometric sillenite phase, $Bi_{12}SiO_{20}$ [47]. That study focused on the bulk response of the ceramic sample, for which an equivalent circuit was proposed that also contained a parallel combination of conducting and dielectric elements. The value of C_x (equivalent to C_2 here) showed a significant decrease with increasing temperature and was attributed to relaxor-like behavior.

Resistance R_3 has higher activation energy than either R_1 or R_2. It clearly represents one feature of the sample-electrode contact impedance but further studies would be required to separate the possible contributions of: electronic conduction; redox reaction associated with oxygen transfer across the interface; Warburg-like impedance associated with diffusion of oxygen molecules towards / away from the interface.

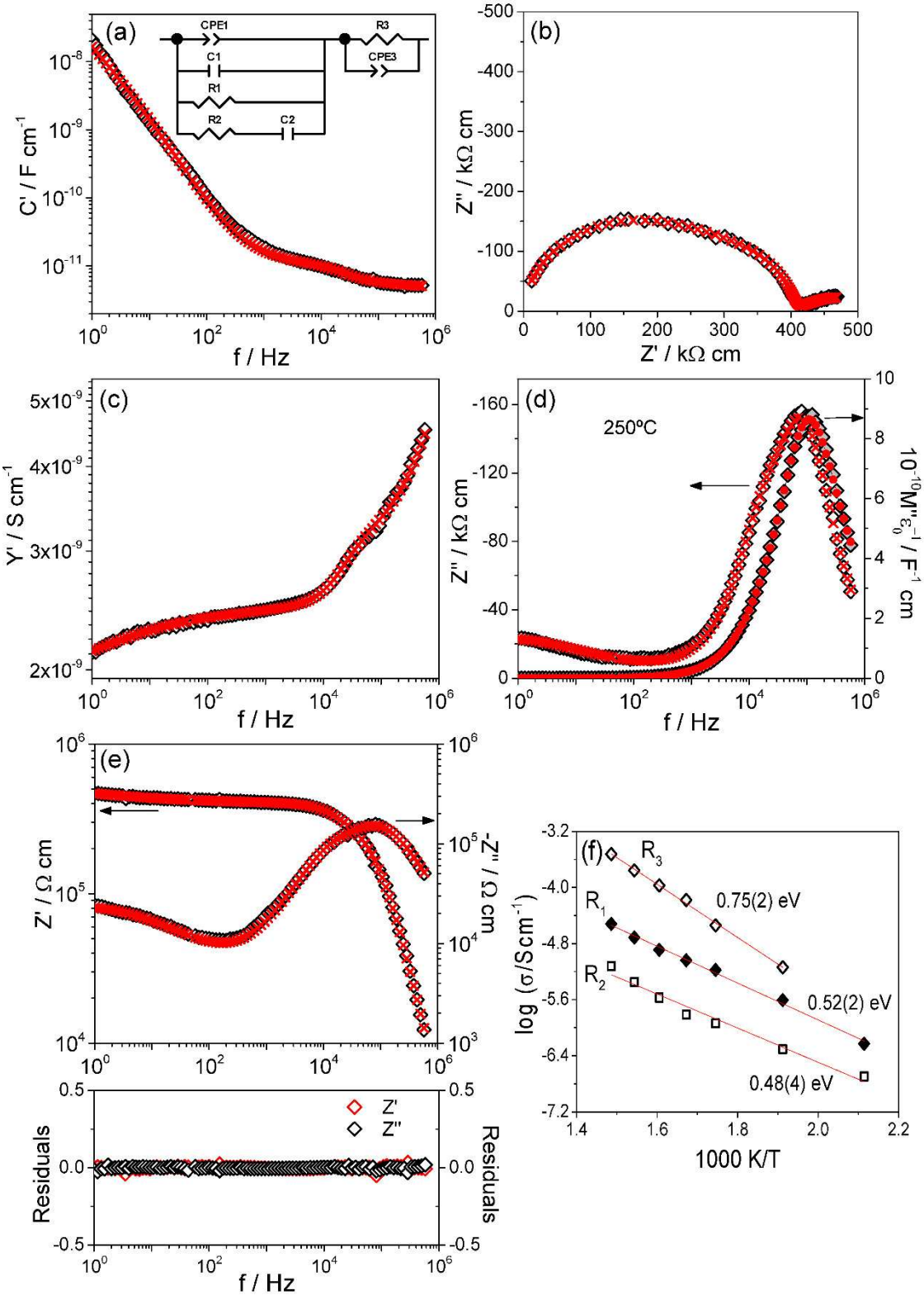

Fig. 9. Fitted and experimental impedance data measured at 250 ºC for $Bi_{25}FeO_{39}$ prepared by mechanosynthesis and sintered at 750 ºC. (a) C' spectroscopic plot, (b) impedance complex plane plot, (c) Y' spectroscopic plot, (d) Z"/M" spectroscopic plots, (e) Z'/Z" spectroscopic plots and residuals, (f) Arrhenius plot for R_1, R_2 and R_3.

In summary, the electrical properties of $Bi_{25}FeO_{39}$ are complex and show clear evidence for mixed conduction of electron holes and oxide ions together with possible relaxor or ferroelectric behavior at temperatures below the measurement temperatures used here.

Similar results and conclusions were obtained for both conventional- and mechano-synthesized samples. The electrical properties are intrinsic to the material, therefore and not dependent on the synthesis conditions.

Table 2. Fitted parameters for the equivalent circuit shown in Fig. 9(a), inset, used to simulate the impedance data for $Bi_{25}FeO_{39}$ prepared by mechanosynthesis and sintered at 750ºC.

T (ºC)	**200**	**250**	**300**	**325**
R_1 (kΩcm)	1.69(1)x10^3	405.6(8)	150.2(2)	109.3(1)
A_1 (pScm^{-1}rad^{-n})	64(12)	93(1)	121(2)	136(3)
n_1	0.69(1)	0.69 (fixed)	0.69 (fixed)	0.69 (fixed)
C_1 (pFcm^{-1})	4.36(9)	4.36 (fixed)	4.36 (fixed)	4.36 (fixed)
C_2 (pFcm^{-1})	7.4(3)	3.5(1)	1.7(1)	1.2(1)
R_2 (kΩcm)	4.7(2)x10^3	2.0(1)x10^3	869(34)	695(42)
A_3 (μScm^{-1}rad^{-n})	--	4.1(2)	6.5(3)	5.2(2)
n_3	--	0.41(1)	0.411 (fixed)	0.411 (fixed)
R_3 (kΩcm)	--	138(8)	34.6(7)	15.0(3)

T (ºC)	**350**	**375**	**400**
R_1 (kΩcm)	77.5(1)	51.7(1)	33.03(3)
A_1 (pScm^{-1}rad^{-n})	131(3)	135(5)	113(4)
n_1	0.69 (fixed)	0.69 (fixed)	0.69 (fixed)
C_1 (pFcm^{-1})	4.36 (fixed)	4.36 (fixed)	4.36 (fixed)
C_2 (pFcm^{-1})	1.2(1)	1.2(5)	1.3 (1)
R_2 (kΩcm)	373(22)	224(15)	124(7)
A_3 (μScm^{-1}rad^{-n})	5.2(2)	5.8(3)	6.4(2)
n_3	0.41 (fixed)	0.41 (fixed)	0.41 (fixed)
R_3 (kΩcm)	9.3(1)	5.7(1)	3.3(1)

3.3 Comparison of conductivity data for Bi ferrites

Arrhenius conductivity plots for the various materials studied here are collected together in Fig. 10. Data are also shown for an insulating sample of $BiFeO_3$ prepared by mechanosynthesis and a leaky sample given a final spark plasma sintering treatment [18, 48]. Conductivity data for the mullite phase, $Bi_4Fe_2O_9$, are more than one order of magnitude less than that of both $BiFeO_3$ samples and therefore, small amounts of this phase would probably not be detected by IS and would not contribute to the conductivity of leaky $BiFeO_3$. The sillenite phase, $Bi_{25}FeO_{39}$, has conductivity values of the same order as those reported for $BiFeO_3$ but much lower activation energy. It seems unlikely, therefore, that the sillenite phase could be responsible for leakage conductivity of $BiFeO_3$.

The sample subjected to SPS treatment, Fig. 10, showed n-type semiconductivity which was subsequently removed by annealing in air at 600 ºC. Under highly reducing conditions, such as in SPS, oxygen loss leading to n-type semiconductivity can occur and may account for the observation in the literature that samples may show n-type behavior and the presence of Fe^{2+} ions [13].

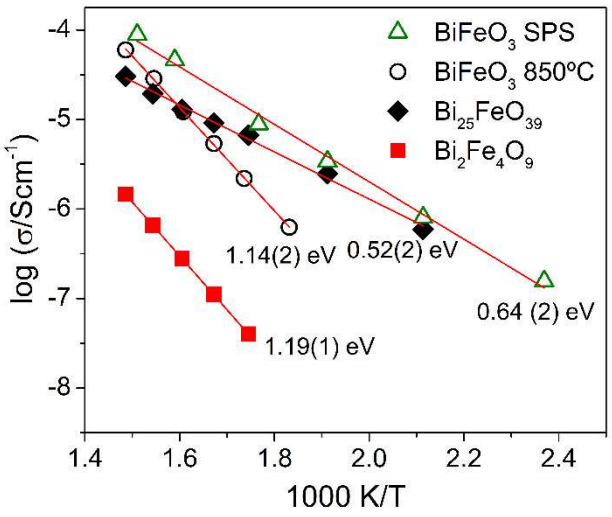

Fig. 10. Arrhenius plots for $Bi_2Fe_4O_9$ annealed in O_2, $Bi_{25}FeO_{39}$ prepared by mechanosynthesis and sintered at 750ºC (R_1), $BiFeO_3$ prepared by mechanosynthesis and sintered at 850ºC [18] and $BiFeO_3$ prepared by mechanosynthesis and sintered by SPS [18].

4. Conclusions

We report a detailed characterization of the electrical properties of two bismuth ferrites, $Bi_2Fe_4O_9$ and $Bi_{25}FeO_{39}$ and conclude that, under normal conditions of synthesis of $BiFeO_3$ at high temperatures in atmospheres of either air or oxygen, these other bismuth ferrite phases are unlikely to be the reason for any leakage conductivity in $BiFeO_3$.

$Bi_2Fe_4O_9$ with a mullite structure has been described in the literature as a multiferroic based on weak, oval-shaped 'ferroelectric' hysteresis loops. Our high frequency impedance measurements show no evidence for a temperature-dependent bulk permittivity, such as would be expected for a ferroelectric material in the Curie-Weiss region above its Curie temperature. The antiferromagnetic properties of $Bi_2Fe_4O_9$ do, however, appear to be well-established.

$Bi_2Fe_4O_9$ is stable on heating in O_2 to 900ºC and is a low conductivity dielectric with intrinsic activation energy 1.19 eV. In atmospheres of lower pO_2, it starts to decompose, as shown by the appearance of Fe_2O_3 in XRD data and an increase in electronic conductivity.

$Bi_{25}FeO_{39}$ with a sillenite structure is a mixed conductor of oxide ions and electronic holes. It also shows evidence of a dielectric relaxation process, as well as long range conduction, which is tentatively attributed to incipient behavior indicative of domain reorientation or relaxor properties at lower temperatures.

Impedance analysis on both materials, $Bi_2Fe_4O_9$ and $Bi_{25}FeO_{39}$, provides much useful information on their electrical properties by careful attention to data analysis and in particular to the choice and fitting of the most appropriate equivalent circuits.

5. Acknowledgements

Financial support from Projects CTQ2014-52763-C2 and CTQ2017-83602-C2 (MINECO-FEDER) is acknowledged. AP thanks VPPI-US for his current contract.

6. References

[1] G. Catalan, J. F. Scott, Physics and Applications of Bismuth Ferrite, Advanced Materials, 21 (24) (2009) 2463-2485. 10.1002/adma.200802849.

[2] W. Eerenstein, N. D. Mathur, J. F. Scott, Multiferroic and magnetoelectric materials, Nature, 442 (7104) (2006) 759-765. 10.1038/nature05023.

[3] M. M. Kumar, V. R. Palkar, K. Srinivas, S. V. Suryanarayana, Ferroelectricity in a pure $BiFeO_3$ ceramic, Applied Physics Letters, 76 (19) (2000) 2764-2766. 10.1063/1.126468.

[4] D. Lebeugle, D. Colson, A. Forget, M. Viret, P. Bonville, J. F. Marucco, S. Fusil, Room-temperature coexistence of large electric polarization and magnetic order in $BiFeO_3$ single crystals, Physical Review B, 76 (2) (2007) 024116. 10.1103/PhysRevB.76.024116.

[5] J. B. Neaton, C. Ederer, U. V. Waghmare, N. A. Spaldin, K. M. Rabe, First-principles study of spontaneous polarization in multiferroic $BiFeO_3$, Physical Review B, 71 (1) (2005) 014113. 10.1103/PhysRevB.71.014113.

[6] N. A. Spaldin, M. Fiebig, The renaissance of magnetoelectric multiferroics, Science, 309 (5733) (2005) 391-392. 10.1126/science.1113357.

[7] T. Zhao, A. Scholl, F. Zavaliche, K. Lee, M. Barry, A. Doran, M. P. Cruz, Y. H. Chu, C. Ederer, N. A. Spaldin, R. R. Das, D. M. Kim, S. H. Baek, C. B. Eom, R. Ramesh, Electrical control of antiferromagnetic domains in multiferroic $BiFeO_3$ films at room temperature, Nature Materials, 5 (10) (2006) 823-829. 10.1038/nmat1731.

[8] D. C. Jia, J. H. Xu, H. Ke, W. Wang, Y. Zhou, Structure and multiferroic properties of $BiFeO_3$ powders, Journal of the European Ceramic Society, 29 (14) (2009) 3099-3103. 10.1016/j.jeurceramsoc.2009.04.023.

[9] M. Muneeswaran, R. Dhanalakshmi, N. V. Giridharan, Structural, vibrational, electrical and magnetic properties of $Bi_{1-x}Pr_xFeO_3$, Ceramics International, 41 (7) (2015) 8511-8519. 10.1016/j.ceramint.2015.03.058.

[10] S. Hunpratub, P. Thongbai, T. Yamwong, R. Yimnirun, S. Maensiri, Dielectric relaxations and dielectric response in multiferroic $BiFeO_3$ ceramics, Applied Physics Letters, 94 (6) (2009) 062904. 10.1063/1.3078825.

[11] R. Mazumder, A. Sen, Effect of Pb-doping on dielectric properties of $BiFeO_3$ ceramics, Journal of Alloys and Compounds, 475 (1) (2009) 577-580. https://doi.org/10.1016/j.jallcom.2008.07.082.

[12] H. Ke, W. Wang, Y. Wang, H. Zhang, D. Jia, Y. Zhou, X. Lu, P. Withers, Dependence of dielectric behavior in $BiFeO_3$ ceramics on intrinsic defects, Journal of Alloys and Compounds, 541 (2012) 94-98. https://doi.org/10.1016/j.jallcom.2012.06.110.

[13] J. G. Wu, Z. Fan, D. Q. Xiao, J. G. Zhu, J. Wang, Multiferroic bismuth ferrite-based materials for multifunctional applications: Ceramic bulks, thin films and nanostructures, Progress in Materials Science, 84 (2016) 335-402. 10.1016/j.pmatsci.2016.09.001.

[14] G. L. Yuan, S. W. Or, Y. P. Wang, Z. G. Liu, J. M. Liu, Preparation and multi-properties of insulated single-phase $BiFeO_3$ ceramics, Solid State Communications, 138 (2) (2006) 76-81. https://doi.org/10.1016/j.ssc.2006.02.005.

[15] Y. P. Wang, L. Zhou, M. F. Zhang, X. Y. Chen, J.-M. Liu, Z. G. Liu, Room-temperature saturated ferroelectric polarization in $BiFeO_3$ ceramics synthesized by rapid liquid phase sintering, Applied Physics Letters, 84 (10) (2004) 1731-1733. 10.1063/1.1667612.

[16] M. S. Bernardo, T. Jardiel, M. Peiteado, A. C. Caballero, M. Villegas, Reaction pathways in the solid state synthesis of multiferroic $BiFeO_3$, Journal of the European Ceramic Society, 31 (16) (2011) 3047-3053. 10.1016/j.jeurceramsoc.2011.03.018.

[17] A. Perejon, P. E. Sanchez-Jimenez, J. M. Criado, L. A. Perez-Maqueda, Thermal Stability of Multiferroic $BiFeO_3$: Kinetic Nature of the beta-gamma Transition and Peritectic Decomposition, Journal of Physical Chemistry C, 118 (45) (2014) 26387-26395. 10.1021/jp507831j.

[18] A. Perejon, N. Maso, A. R. West, P. E. Sanchez-Jimenez, R. Poyato, J. M. Criado, L. A. Perez-Maqueda, Electrical Properties of Stoichiometric $BiFeO_3$ Prepared by Mechanosynthesis with Either Conventional or Spark Plasma Sintering, Journal of the American Ceramic Society, 96 (4) (2013) 1220-1227. 10.1111/jace.12186.

[19] A. Perejon, P. E. Sanchez-Jimenez, L. A. Perez-Maqueda, J. M. Criado, J. R. de Paz, R. Saez-Puche, N. Maso, A. R. West, Single phase, electrically insulating, multiferroic La-substituted $BiFeO_3$ prepared by mechanosynthesis, Journal of Materials Chemistry C, 2 (39) (2014) 8398-8411. 10.1039/c4tc01426j.

[20] I. Szafraniak, M. Polomska, B. Hilczer, A. Pietraszko, L. Kepinski, Characterization of $BiFeO_3$ nanopowder obtained by mechanochemical synthesis, Journal of the European Ceramic Society, 27 (13-15) (2007) 4399-4402. 10.1016/j.jeurceramsoc.2007.02.163.

[21] D. C. Craig, N. C. Stephenson, Structural studies of some body-centered cubic phases of mixed oxides involving Bi_2O_3: The structures of $Bi_{25}FeO_{40}$ and $Bi_{38}ZnO_{60}$, Journal of Solid State Chemistry, 15 (1) (1975) 1-8. https://doi.org/10.1016/0022-4596(75)90264-9.

[22] Y. Chen, Q. Wu, J. Zhao, Selective synthesis on structures and morphologies of $Bi_xFe_yO_z$ nanomaterials with disparate magnetism through time control, Journal of Alloys and Compounds, 487 (1) (2009) 599-604. https://doi.org/10.1016/j.jallcom.2009.08.022.

[23] C. A. Scurti, N. Auvray, M. W. Lufaso, S. Takeda, H. Kohno, D. J. Arenas, Electron diffraction study of the sillenites $Bi_{12}SiO_{20}$, $Bi_{25}FeO_{39}$ and $Bi_{25}InO_{39}$: Evidence of short-range ordering of oxygen-vacancies in the trivalent sillenites, Aip Advances, 4 (8) (2014) 087125. 10.1063/1.4893341.

[24] M. Devalette, N. Khachani, G. Meunier, P. Hagenmuller, Simulated behavior of bismuth oxide in the formation of some $Bi_{12}[A_{\alpha+x}Bi_{\beta+V}]O_{20}$ sillenite-type phases, Materials Letters, 2 (4, Part B) (1984) 318-319. https://doi.org/10.1016/0167-577X(84)90043-0.

[25] R. Köferstein, T. Buttlar, S. G. Ebbinghaus, Investigations on $Bi_{25}FeO_{40}$ powders synthesized by hydrothermal and combustion-like processes, Journal of Solid State Chemistry, 217 (2014) 50-56. https://doi.org/10.1016/j.jssc.2014.05.006.

[26] T. Guo-Qiang, Z. Yu-Qin, M. Hong-Yan, X. Ao, R. Hui-Jun, Controllable Microwave Hydrothermal Synthesis of Bismuth Ferrites and Photocatalytic Characterization, Journal of the American Ceramic Society, 95 (1) (2012) 280-289. doi:10.1111/j.1551-2916.2011.04775.x.

[27] Y. Dai, L. Yin, Low Fe-doped Bi_2O_3 photocatalyst with long wavelength response: Crystalline transition and mechanisms by first-principles calculation, Journal of Alloys and Compounds, 563 (2013) 80-84. https://doi.org/10.1016/j.jallcom.2013.02.105.

[28] M. T. Borowiec, A. Majchrowski, J. Zmija, H. Szymczak, T. Zayarniuk, E. Michalski, M. Baranski, in *Solid State Crystals 2002: Crystalline Materials for Optoelectronics*, eds.

J. Rutkowski, A. Rogalski, Spie-Int Soc Optical Engineering, Bellingham, 2003, pp. 26-30.

[29] A. A. Zatsiupa, L. A. Bashkirov, I. O. Troyanchuk, G. S. Petrov, A. I. Galyas, L. S. Lobanovsky, S. V. Truhanov, Magnetization, magnetic susceptibility, effective magnetic moment of Fe^{3+} ions in $Bi_{25}FeO_{39}$ ferrite, Journal of Solid State Chemistry, 212 (2014) 147-150. https://doi.org/10.1016/j.jssc.2014.01.019.

[30] W. Lei, D. Chunhui, C. Hang, Y. Jinli, J. Changjun, X. Desheng, Hydrothermal Synthesis and Magnetic Properties of Bismuth Ferrites Nanocrystals with Various Morphology, Journal of the American Ceramic Society, 95 (12) (2012) 3922-3927. doi:10.1111/j.1551-2916.2012.05419.x.

[31] Y. Xiong, M. Z. Wu, Z. M. Peng, N. Jiang, Q. W. Chen, Hydrothermal synthesis and characterization of $Bi_2Fe_4O_9$ nanoparticles, Chemistry Letters, 33 (5) (2004) 502-503. 10.1246/cl.2004.502.

[32] A. K. Singh, S. D. Kaushik, B. Kumar, P. K. Mishra, A. Venimadhav, V. Siruguri, S. Patnaik, Substantial magnetoelectric coupling near room temperature in $Bi_2Fe_4O_9$, Applied Physics Letters, 92 (13) (2008) 132910. 10.1063/1.2905815.

[33] M. Liu, H. Yang, Y. Lin, Y. Yang, Influence of Co doping on the magnetic properties of $Bi_2Fe_4O_9$ powders, Journal of Materials Science: Materials in Electronics, 25 (11) (2014) 4949-4953. 10.1007/s10854-014-2256-9.

[34] Z. M. Tian, S. L. Yuan, X. L. Wang, X. F. Zheng, S. Y. Yin, C. H. Wang, L. Liu, Size effect on magnetic and ferroelectric properties in $Bi_2Fe_4O_9$ multiferroic ceramics, Journal of Applied Physics, 106 (10) (2009) 103912. 10.1063/1.3259392.

[35] Y. A. Park, K. M. Song, K. D. Lee, C. J. Won, N. Hur, Effect of antiferromagnetic order on the dielectric properties of $Bi_2Fe_4O_9$, Applied Physics Letters, 96 (9) (2010) 092506. 10.1063/1.3339880.

[36] S. Huang, Y. Qiu, S. L. Yuan, Enhanced magnetization and electric polarization in $Bi_2Fe_4O_9$ ceramics by magnetic field pre-sintering, Materials Letters, 160 (2015) 323-326. 10.1016/j.matlet.2015.08.014.

[37] B. Hu, J. F. Wang, J. Zhang, Z. B. Gu, S. T. Zhang, Synthesis, structures and properties of single phase $BiFeO_3$ and $Bi_2Fe_4O_9$ powders by hydrothermal method, Journal of Materials Science-Materials in Electronics, 26 (9) (2015) 6887-6891. 10.1007/s10854-015-3305-8.

[38] Z. Irshad, S. H. Shah, M. A. Rafiq, M. M. Hasan, First principles study of structural, electronic and magnetic properties of ferromagnetic $Bi_2Fe_4O_9$, Journal of Alloys and Compounds, 624 (2015) 131-136. 10.1016/j.jallcom.2014.10.174.

[39] K. J. D. MacKenzie, T. Dougherty, J. Barrel, The electronic properties of complex oxides of bismuth with the mullite structure, Journal of the European Ceramic Society, 28 (2) (2008) 499-504. 10.1016/j.jeurceramsoc.2007.03.012.

[40] Q. Zhang, W. Gong, J. Wang, X. Ning, Z. Wang, X. Zhao, W. Ren, Z. Zhang, Size-Dependent Magnetic, Photoabsorbing, and Photocatalytic Properties of Single-Crystalline $Bi_2Fe_4O_9$ Semiconductor Nanocrystals, The Journal of Physical Chemistry C, 115 (51) (2011) 25241-25246. 10.1021/jp208750n.

[41] Q.-J. Ruan, W.-D. Zhang, Tunable Morphology of $Bi_2Fe_4O_9$ Crystals for Photocatalytic Oxidation, The Journal of Physical Chemistry C, 113 (10) (2009) 4168-4173. 10.1021/jp810098f.

[42] S. R. Mohapatra, B. Sahu, T. Badapanda, M. S. Pattanaik, S. D. Kaushik, A. K. Singh, Optical, dielectric relaxation and conduction study of $Bi_2Fe_4O_9$ ceramic, Journal of Materials Science-Materials in Electronics, 27 (4) (2016) 3645-3652. 10.1007/s10854-015-4203-9.

[43] Z. R. Kann, J. T. Auletta, E. W. Hearn, S. U. Weber, K. D. Becker, H. Schneider, M. W. Lufaso, Mixed crystal formation and structural studies in the mullite-type system $Bi_2Fe_4O_9$-$Bi_2Mn_4O_{10}$, Journal of Solid State Chemistry, 185 (2012) 62-71. 10.1016/j.jssc.2011.10.046.

[44] S. F. Radaev, L. A. Muradyan, V. I. Simonov, Atomic-structure and crystal-chemistry of sillenites - $Bi_{12}(Bi^{3+}0.50Fe^{3+}0.50)O_{19.50}$ and $Bi_{12}(Bi^{3+}0.67Zn^{2+}0.33)O_{19.33}$, Acta Crystallographica Section B-Structural Science, 47 (1991) 1-6. 10.1107/s0108768190007492.

[45] N. Maso, A. R. West, Electronic Conductivity in Yttria-Stabilized Zirconia under a Small dc Bias, Chemistry of Materials, 27 (5) (2015) 1552-1558. 10.1021/cm503957x.

[46] M. A. Hernandez, A. R. West, Dipolar relaxation and impedance of an yttria-stabilised zirconia ceramic electrolyte, Journal of Materials Chemistry A, 4 (4) (2016) 1298-1305. 10.1039/c5ta08990e.

[47] Y. Hu, D. C. Sinclair, Relaxor-like Dielectric Behavior in Stoichiometric Sillenite $Bi_{12}SiO_{20}$, Chemistry of Materials, 25 (1) (2013) 48-54. 10.1021/cm3031363.

[48] A. Perejon, P. E. Sanchez-Jimenez, R. Poyato, N. Maso, A. R. West, J. M. Criado, L. A. Perez-Maqueda, Preparation of phase pure, dense fine grained ceramics by conventional and spark plasma sintering of La-substituted $BiFeO_3$ nanoparticles, Journal of the European Ceramic Society, 35 (8) (2015) 2283-2293. 10.1016/j.jeurceramsoc.2015.01.030.